

Thermal, vibrational, and thermoelastic properties of $Y_2Mo_3O_{12}$ and their relations to negative thermal expansion

Carl P. Romao,¹ Kimberly J. Miller,¹ Michel B. Johnson,¹ J. W. Zwanziger,¹ Bojan A. Marinkovic,² and Mary Anne White^{1,*}

¹*Department of Chemistry and Institute for Research in Materials, Dalhousie University, Halifax, Nova Scotia, B3H 4R2, Canada*

²*Departamento de Engenharia de Materiais, Pontifícia Universidade Católica de Rio de Janeiro (PUC-Rio),*

Rua Marquês de São Vicente 225, Gávea, RJ, Brasil

(Received 20 March 2014; revised manuscript received 29 April 2014; published 21 July 2014)

$Y_2Mo_3O_{12}$, a material that exhibits negative thermal expansion (NTE) from 10 to 1173 K, offers an excellent opportunity to examine relationships between NTE and other physical properties over a wide temperature range. We report experimental heat capacity, thermal conductivity, and elastic properties of $Y_2Mo_3O_{12}$, as well as results of an *ab initio* study of the lattice dynamics, and show how the anomalously high heat capacity and low thermal conductivity are correlated with NTE. We also report the *ab initio* elastic tensor and experimental velocity of sound of $Y_2Mo_3O_{12}$ and use it to calculate the thermal stresses in a simulated polycrystal using finite-element analysis, showing that elastic anisotropy and thermal expansion anisotropy couple to influence the properties of the bulk solid.

DOI: [10.1103/PhysRevB.90.024305](https://doi.org/10.1103/PhysRevB.90.024305)

PACS number(s): 63.20.-e, 65.40.-b

I. INTRODUCTION

Materials that exhibit the unusual property of negative thermal expansion (NTE), also known as thermomiotic materials [1], are of interest scientifically and for a wide range of applications. The former motivation includes a desire to advance understanding of the relationship between structure, including dynamics, and physical properties, with the goal of tailoring specific properties of materials. Potential applications include development of materials with particular thermal expansion values, for example, to mitigate thermally induced buckling and thermal shock fracture. Recent reviews highlight the importance and challenges of research concerning thermomiotic materials [1,2].

Many thermomiotic materials have open framework structures. The most studied thermomiotic material is ZrW_2O_8 , which exhibits NTE over the temperature range 0.3 to 1050 K [3]. The largest family of thermomiotic materials has the formula unit $A_2M_3O_{12}$ (with A as a rare earth or other trivalent metal cation and M as Mo^{6+} or W^{6+}) and exhibits monoclinic ($P2_1/a$) and orthorhombic ($Pbcn$) structures with AO_6 octahedra connected through vertex oxygen atoms to MO_4 tetrahedra. There are indications that the unusual ease of polyhedral distortion is responsible for thermomiotic behavior in $A_2M_3O_{12}$ [4–6]. $A_2M_3O_{12}$ materials are of special interest because the relative ease of substitution of the A cation allows for highly tunable properties [1].

Like ZrW_2O_8 , $Y_2Mo_3O_{12}$ is known to be thermomiotic over a broad temperature range (10 to 1173 K) [5,7]. Unlike many other $A_2M_3O_{12}$ materials [1], $Y_2Mo_3O_{12}$ does not undergo a temperature-induced phase transition out of its thermomiotic orthorhombic phase upon cooling. This allows determination of its thermal properties at low temperature, as well as direct applicability of the results of density functional theory (DFT) calculations based on the electronic structure at 0 K. These qualities, in addition to its structure being determined [5] and being considered to be the parent compound of the near-zero

thermal expansion $In(HfMg)_{0.5}Mo_3O_{12}$ [8], make $Y_2Mo_3O_{12}$ a good candidate for investigation both experimentally and by theoretical approaches. The electronic and phononic densities of states of $Y_2Mo_3O_{12}$, as calculated by DFT, have recently been published [6].

To understand thermomiotic materials at a deeper level requires information about their structures, dynamics, and thermal and elastic behaviors. Although it is possible to advance understanding of the phononic interactions of these materials through experiments, such as inelastic neutron scattering or vibrational spectroscopy, the absence of single crystals of thermomiotic molybdate materials prevents full experimental investigations of the associated elastic properties. Theoretical methods can be very revealing concerning both phonons and elasticity, and here we take a DFT approach to investigate $Y_2Mo_3O_{12}$. We validate the theoretical phonon results by experimental heat capacity and elasticity measurements. In addition, we present experimental results for the thermal conductivity of $Y_2Mo_3O_{12}$. The latter is especially important because the NTE-inducing low-frequency optic modes associated with framework structures also have been associated with low thermal conductivity in ZrW_2O_8 [9], $HfMo_2O_8$ [10], and $HfMgMo_3O_{12}$ [11]. If low thermal conductivity is a general phenomenon in thermomiotic materials, applications of such materials would require special consideration regarding thermal management. Armed with a detailed understanding of phonon behavior and data for thermal conduction and mechanical properties of $Y_2Mo_3O_{12}$, we then use finite-element modeling to understand thermal stress and shock in this material.

II. METHODS

A. Sample preparation

$Y_2Mo_3O_{12}$ was synthesized from the solid-state reaction of a stoichiometric mixture of MoO_3 and Y_2O_3 . Samples used for heat capacity and thermal conductivity determinations were prepared, as described in Ref. [5]. Under ambient conditions, $Y_2Mo_3O_{12}$ readily absorbs moisture from the air; this water

*Corresponding author: mary.anne.white@dal.ca

TABLE I. Thickness and density of the 2.8-mm-diameter $Y_2Mo_3O_{12}$ pellets used for thermal conductivity measurements.

Sample	Thickness (mm)	Density ($g\ cm^{-1}$)	% theoretical density
$Y_2Mo_3O_{12}$ (E1)	0.91	2.02	63
$Y_2Mo_3O_{12}$ (E2)	1.57	2.11	67
$Y_2Mo_3O_{12}$ (E3)	0.91	1.92	61

is incorporated into the lattice, inhibits the rocking motion of the tetrahedra, and destroys the *Pbcn* framework responsible for thermomiotic behavior [5,7,12,13]. Due to the extremely hygroscopic nature of this material, appropriate dehydration, sample preparation, handling, and storage were essential to obtain high-quality measurements of the thermal properties of the thermomiotic phase below 300 K [5].

Pellets for thermal conductivity measurements were prepared by mixing water with $Y_2Mo_3O_{12}$ powder until tacky, compacting to 2.8-mm-diameter pellets under ≈ 0.5 GPa of pressure, followed by sintering in air for 12 h at 1063 K using a heating ramp up of $5\ K\ min^{-1}$, before quenching to room temperature. Samples were stored in a desiccator until used. Details of the thermal conductivity samples are presented in Table I.

Samples for ultrasonic measurements were prepared by ball milling a stoichiometric mixture of Y_2O_3 (Acros Organics, 99.99%) and MoO_3 (Sigma Aldrich, $\geq 99.5\%$) for 12 h, pressing the milled powder in a 15-mm-diameter die under ≈ 55 MPa of pressure and sintering for 24 h at 1223 K, using a temperature ramp up of $5\ K\ min^{-1}$ and natural cooling. To avoid hydration of the samples, they were sintered in Ar atmosphere and then immediately placed in a desiccator. Details of the pellets used for ultrasonic studies are presented in Table II.

The phase purity of each $Y_2Mo_3O_{12}$ sample was confirmed as $>99\%$ by x-ray powder diffraction. The heat capacity and thermal conductivity samples showed negligible water content (differential scanning calorimetry showed water below the limit of detection, i.e., $<0.1\ mol\%$ water).

B. Experimental methods

Heat capacity measurements were conducted using the relaxation calorimetry method, with a Physical Property Measurement System (PPMS) model 6000 from Quantum Design. The additional precautions required by the hygroscopic nature of the sample are described in detail elsewhere [5]. To achieve high-accuracy heat capacity measurements with

TABLE II. Dimensions and densities of the $Y_2Mo_3O_{12}$ pellets used to measure the longitudinal and transverse velocities of sound.

Sample	Diameter (mm)	Thickness (mm)	Density ($g\ cm^{-1}$)	% theoretical density
$Y_2Mo_3O_{12}$ (U1)	13.22	3.52	2.72	87
$Y_2Mo_3O_{12}$ (U2)	13.02	3.56	2.65	85
$Y_2Mo_3O_{12}$ (U3)	13.07	3.53	2.72	87

relaxation calorimetry, it has been recommended that several different sample masses be measured [14]. The $Y_2Mo_3O_{12}$ samples measured here ranged from 4.94 to 13.94 mg. Samples generally contributed $>40\%$ to the total heat capacity (except the 4.94 mg sample that gave only about half that contribution but provided a check on potential thermal lag). The thermal coupling of the samples to the platform was excellent throughout ($>80\%$ for all but the 4.94 mg sample).

Thermal conductivity was determined by a power-pulse method, in vacuum ($P < 10^{-5}$ Torr), using the thermal transport option of the PPMS. We used a two-probe configuration, in which the heater and hot thermometer shared one lead, and the cold foot and cold thermometer shared the other lead. Cylindrical samples of $Y_2Mo_3O_{12}$ were secured between two gold-plated copper leads with a thin layer of silver-loaded epoxy (Tra-Bond 2902). Prior to measurement, the samples were preheated to 380 K under high vacuum to remove any traces of water from $Y_2Mo_3O_{12}$, and the thermal conductivity was determined from 300 to 2 K. A modulated heater current generated a one-dimensional heat flux across the sample, and the temperature response was monitored, while the cryostat temperature was slewed at a constant slow rate ($0.75\ K\ min^{-1}$), and measurements were taken continuously, as parameters were adjusted to optimize the measurements [15]. This method can give results in excellent agreement with the slower but more direct stepwise mode [9]. Following corrections for radiative losses and conduction due to the thermometry and shoe assembly, the sample conductance was obtained and subsequently converted to thermal conductivity (κ) by taking into account the sample geometry.

The longitudinal and transverse velocities of sound of $Y_2Mo_3O_{12}$ were determined by ultrasonic measurement of three sintered $Y_2Mo_3O_{12}$ pellets using a Panametrics ultrasonic thickness gage. Panametrics shear-wave couplant was used for the transverse measurement, and due to the roughness of the sample surface, anhydrous glycerol was used as the couplant for the longitudinal measurement. The measurements were performed in a dry N_2 atmosphere.

C. Theoretical methods

First-principles calculations of the response of $Y_2Mo_3O_{12}$ to various perturbations were performed using the ABINIT software package [16,17]. The ABINIT code is a common project of the Université Catholique de Louvain, Corning Incorporated, and other contributors [18]. This code implements Kohn-Sham DFT using a plane-wave basis and pseudopotentials. A similar approach had proven insightful concerning NTE in cyanides [19]. Here, the orthorhombic structure of $Y_2Mo_3O_{12}$ published by Marinkovic *et al.* [7] was used; it has 68 atoms in the unit cell ($Z = 4$). The Perdew-Burke-Ernzerhof (PBE) exchange and correlation functional [20] and two-projector optimized norm-conserving Vanderbilt pseudopotentials [21] were used. These pseudopotentials were validated in computations on bulk Y, bulk Mo, and Y_2O_3 . Relaxed lattice constants within 1% of experiment were obtained, and bulk moduli very close to experiment, in the worst case (Y_2O_3) 7% greater than experiment. A 25 Hartree cutoff was used for the plane-wave basis, and a $2 \times 3 \times 3$ Monkhorst-Pack grid was used to sample reciprocal space.

The experimental cell parameters yielded an internal stress of about -1 GPa with the above parameters, which was relaxed to less than 10^{-3} GPa. This procedure led to an increase of cell parameters of several percent, typical of generalized gradient approximation (GGA) functionals. The electronic band structure was computed for the relaxed cell. Finally, the response to electric field, strain, and atomic displacement perturbations were computed using the density functional perturbation theory implementation in ABINIT.

D. Finite-element analysis

The DFT stiffness tensor¹ and experimental thermal expansion tensor were used to perform a finite-element analysis (COMSOL Multiphysics, v. 4.2 [24]) of the thermal stresses arising upon cooling a polycrystalline sample of $Y_2Mo_3O_{12}$. The models used consisted of 64 randomly oriented cubic crystallites of $Y_2Mo_3O_{12}$ arranged in a larger cubic polycrystal. The mesh consisted of cubic elements, with each crystallite being composed of 64 elements. The mesh size was checked by a mesh convergence study. To sample a large number of potential orientations, 400 models, each with a different set of random orientations of the crystallites, were used. The results presented herein, therefore, are representative of the microstructural stress distributions which can be caused by grain misalignment.

Roller boundary conditions were applied along three orthogonal sides of the polycrystal, while the other three sides of the cube were left unconstrained. A 700 K temperature drop was imposed at these boundaries of the model to mimic thermal stress in the material. The unconstrained sides reduce the average stress in the polycrystal [25]; however, this approach was required to determine the effect of elastic anisotropy on the thermal expansion (see below). The results of the finite-element analysis should, therefore, be considered to be qualitatively accurate, which is informative because their main purpose is to compare the stresses to each other.

III. RESULTS AND DISCUSSION

A. Electronic properties

The band structure calculation predicts $Y_2Mo_3O_{12}$ to be an indirect gap insulator, with a band gap of about 3.6 eV at $T = 0$ K. The bands in $Y_2Mo_3O_{12}$ are relatively dispersionless, as might be expected in such a complex unit cell. The calculated low- and high-frequency dielectric properties are reported in Table III.

¹The elastic tensor used in the finite-element analysis presented here was calculated using the methodology described above but with norm-conserving pseudopotentials generated by the Opium code [22]. The resulting elastic tensor is shown in Eq. (S5) in the Supplemental Material [23]. Three finite-element models were analyzed using the elastic tensor of Eq. (1) as well as that of Eq. (S5) and showed a decrease in stress of approximately 10% between the models using Eqs. (1) and (S5).

TABLE III. Dielectric tensor of $Y_2Mo_3O_{12}$ in the low- and high-frequency limits.

Direction	ϵ_0	ϵ_∞
x	4.60	2.87
y	7.52	2.95
z	7.64	2.91

B. Computation of vibrational modes

Vibrational modes were computed using density functional perturbation theory within the ABINIT software package. Strictly, this approach computes the second derivative of energy with respect to atomic displacements and then constructs the phonon modes through linear combinations. Computational effort was minimized by calculating only one of the symmetry-related modes. Phonon q points were sampled using the same $2 \times 3 \times 3$ Monkhorst-Pack scheme as for the electronic structure, and then frequencies at arbitrary q points were obtained through interpolation from the resulting dynamical database, using the anadbb facility of the ABINIT package. Because of inherent finite sampling errors, the interatomic force constants computed as above and the computed effective charges are constrained by an acoustic sum rule. We estimate the phonon frequencies computed here to be converged to well within a percent, while by using the PBE functional in an insulator such as this with simple electronic structure, we would expect the frequencies to match experiment to within 5 to 10%. The computed phonon density of states is shown in Fig. 1. It is comparable to that previously reported by L. Wang *et al.* [6], although they reported a lower contribution due to the O atoms.

The detailed results, shown in the Supplemental Material, Table S1, and Figs. S1 and S2 [23], in comparison with the experimental Raman spectrum [26], show reasonable agreement between the calculated and measured vibrational energies.

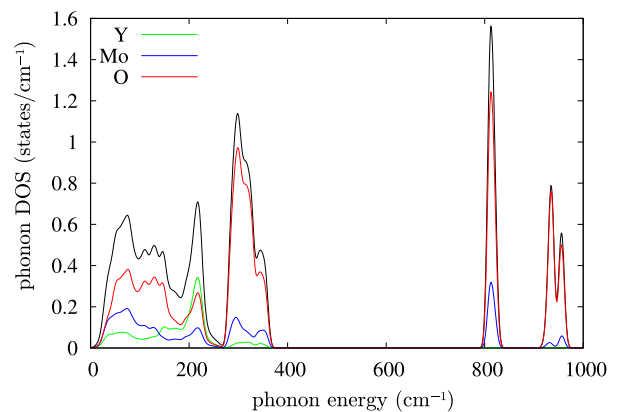


FIG. 1. (Color online) The calculated phonon density of states of $Y_2Mo_3O_{12}$, showing contributions from the Y, Mo, and O atoms. Sampling was performed using 1 cm^{-1} bins.

TABLE IV. Axial elastic constants for $Y_2Mo_3O_{12}$.

Young's modulus (GPa)		Shear modulus (GPa)		Compressibility (GPa^{-1})		Poisson ratio	
E_{11}	57.6	G_{23}	26.6	β_{11}	1.04×10^{-2}	ν_{23}	0.572
E_{22}	49.8	G_{13}	13.5	β_{22}	5.97×10^{-3}	ν_{13}	0.252
E_{33}	44.1	G_{12}	14.7	β_{33}	5.36×10^{-3}	ν_{12}	0.134

C. Elastic properties

The elastic tensor C of $Y_2Mo_3O_{12}$ was calculated from the density functional perturbation theory results to be

$$C = \begin{pmatrix} 68.3 & 23.4 & 27.9 & 0 & 0 & 0 \\ 23.4 & 82.2 & 49.6 & 0 & 0 & 0 \\ 27.9 & 49.6 & 77.2 & 0 & 0 & 0 \\ 0 & 0 & 0 & 26.6 & 0 & 0 \\ 0 & 0 & 0 & 0 & 13.5 & 0 \\ 0 & 0 & 0 & 0 & 0 & 14.7 \end{pmatrix} \times \text{GPa}. \quad (1)$$

The components of the elastic tensor can be converted to the axial Young's moduli, shear moduli, compressibilities, and Poisson ratios [27]; these are shown in Table IV.

For reference, the thermal expansion tensor α of $Y_2Mo_3O_{12}$ (100 to 900 K) is [5,7]

$$\alpha = \begin{pmatrix} 2.3 & 0 & 0 \\ 0 & -13 & 0 \\ 0 & 0 & -17 \end{pmatrix} \times 10^{-6} \text{ K}^{-1}. \quad (2)$$

It can be seen that the axial coefficient of thermal expansion (CTE) is positively correlated with the axial Young's modulus; however, there is also a positive correlation with the axial compressibility due to the high value of G_{23} . The trend in axial compressibility is similar to that reported for the structurally related material $Sc_2W_3O_{12}$ ($\beta_{11} = 6.32 \times 10^{-3} \text{ GPa}^{-1}$, $\beta_{22} = 1.76 \times 10^{-2} \text{ GPa}^{-1}$, $\beta_{33} = 6.84 \times 10^{-3} \text{ GPa}^{-1}$; $\alpha_{11} = -6.3 \times 10^{-5} \text{ \AA K}^{-1}$, $\alpha_{22} = 7.5 \times 10^{-5} \text{ \AA K}^{-1}$, and $\alpha_{33} = -5.5 \times 10^{-5} \text{ \AA K}^{-1}$) [28,29].

The transverse and longitudinal velocities of sound were determined experimentally to validate the calculated elastic constants. The measured velocities of sound were corrected for porosity as follows [30]:

$$v = v_0(1 - \varphi), \quad (3)$$

where v is the measured velocity, v_0 is the corrected, fully densified velocity, and φ is the pore fraction. This model assumes that the particles are spherical, but the pore fraction in these $Y_2Mo_3O_{12}$ samples is small enough ($\approx 15\%$) that error introduced by this assumption should be small.

The sound velocities corrected to bulk density were found to be $v_l = 3.4 \pm 0.1$ and $v_t = 2.0 \pm 0.1 \text{ m s}^{-1}$.² From these measurements, the bulk and shear moduli were derived as 21 ± 3 and $12 \pm 1 \text{ GPa}$, respectively. Because these measurements were made on sintered powder samples, it is appropriate to compare them to the DFT calculations after isotropic averaging. Using the Voigt-Reuss-Hill procedure on the elastic

tensor determined from DFT yields 46.8 and 18.5 GPa for the bulk and shear moduli. Because of the discrepancy between these values and the experimental ones, the elastic properties were recalculated from DFT using a finite strain difference method rather than the density functional perturbation theory approach. Essentially, the same computational results were obtained. On the other hand, we note that the calculations are effectively at $T = 0 \text{ K}$ while the experiments were at room temperature, and at least one other wide-range NTE material, ZrW_2O_8 , shows very marked temperature dependence in the elastic properties, stiffening by some 40% over this temperature range [31]. Similar behavior in $Y_2Mo_3O_{12}$ would account for most of the difference between the two approaches.

To validate our experimental ultrasonic methodology, the bulk modulus of $Sc_2W_3O_{12}$ was measured and compared with the literature value from high-pressure x-ray diffraction. Three pellets with an average of 78.6% of the theoretical density were used. The measured bulk modulus was found to be $35 \pm 4 \text{ GPa}$, which compares well to the literature value of 31 GPa [28].

D. Lattice dynamical contribution to the heat capacity

The experimental heat capacity of $Y_2Mo_3O_{12}$, shown in Fig. 2 (see Supplemental Material [23] for data), is smooth over the temperature range 2 to 300 K, indicating an absence of phase transitions [5].

A very simple approximation of the heat capacity is the constituent additivity approach, whereby $C_{P,m}(Y_2Mo_3O_{12})$ is assessed in comparison with $C_{P,m}(Y_2O_3) + 3C_{P,m}(MoO_3)$. Although this method works very well for many inorganic materials [32], here it falls short of the experimental heat capacity, especially for $T < 150 \text{ K}$ (see Supplemental

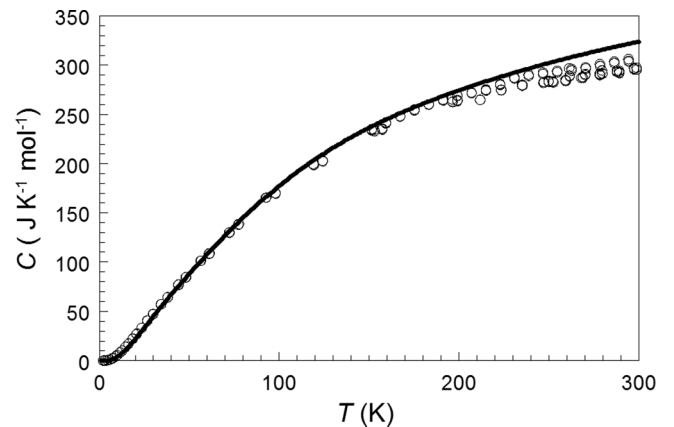


FIG. 2. Heat capacity of $Y_2Mo_3O_{12}$: \circ , experimental $C_{P,m}$; black line is calculated $C_{P,m}$ from the phonon density of states over the full Brillouin zone.

²Standard errors are given at the 95% confidence level.

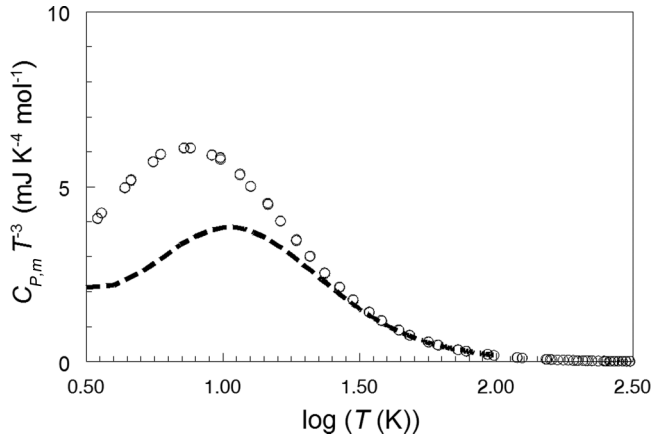


FIG. 3. Low-temperature heat capacity of $\text{Y}_2\text{Mo}_3\text{O}_{12}$, expressed as $C_{P,m} T^{-3}$, as a function of temperature: \circ , experimental $C_{P,m}$ data ($C_P \cong C_V$ in this temperature range); dashed line is calculated $C_{V,m}$ from DFT, including dispersion.

Material [23]), due to the low-frequency modes that are associated with the open framework of $\text{Y}_2\text{Mo}_3\text{O}_{12}$ and not present in Y_2O_3 or MoO_3 .

We used the experimental heat capacity data to validate the phonon modes from the DFT calculations. The as-measured molar heat capacity is at constant pressure, $C_{P,m}$ where the $(C_{P,m} - C_{V,m})$ term accounting for thermal expansion was assessed here using the direction-dependent experimental thermal expansion values [5,7] and the full tensor relationship with the elastic constants from our DFT calculations. (This term is a very small contributor to the total heat capacity.) The comparison between $C_{P,m}$ from experiment and from the full Brillouin zone calculation is excellent, validating the DFT results. The calculation without dispersion (i.e., using the Γ -point frequencies for the optical modes) also is good but does not provide as accurate a representation at low temperatures as the full Brillouin zone calculation (see Supplemental Material [23] for details).

The heat capacity at low temperatures ($T < 50$ K) is very sensitive to the presence of low-frequency modes in many thermomiotic materials. The heat capacities of several thermomiotic materials have been shown to be anomalously high at low temperatures [9,11,33] rather than following Debye-like T^3 behavior ($C_{P,m} \propto T^3$), and this is the case also for $\text{Y}_2\text{Mo}_3\text{O}_{12}$ (Fig. 3). The low-frequency optic modes with significant dispersion (see Supplemental Material, Fig. S2 [23]) that contribute to the heat capacity at low temperature and are responsible for the heat capacity anomaly most likely contribute to NTE because all vibrational modes with energies below 140 cm^{-1} in $\text{Y}_2\text{Mo}_3\text{O}_{12}$ have been reported to have negative Grüneisen parameters [6]. Here, we can see (Fig. 1) the presence of low-frequency modes in $\text{Y}_2\text{Mo}_3\text{O}_{12}$, and that these modes are disproportionately associated with the Mo atoms.

The present calculated heat capacity including dispersion shows excellent agreement with the experimental data and the presence of a low-temperature peak in $C_{P,m}/T^3$ but of slightly lower magnitude than the experiment (Fig. 3).

E. Thermal conductivity

The temperature-dependent thermal conductivities, κ , for three independent samples of $\text{Y}_2\text{Mo}_3\text{O}_{12}$ were determined (data in the Supplemental Material [23]), and the values scaled up to full density using Klemens' model ($\kappa = \kappa_m(1 - (4\varphi/3))$), where κ_m is the fully densified thermal conductivity and φ is again the pore fraction) [34]. We have shown that the Klemens' treatment of polycrystalline data can accurately predict thermal conductivity of single-crystal samples above ~ 30 K [35].

Figure 4 shows the fully densified thermal conductivity data for $\text{Y}_2\text{Mo}_3\text{O}_{12}$. The thermal conductivity is low and glasslike, despite the crystalline structure of $\text{Y}_2\text{Mo}_3\text{O}_{12}$. Indeed, it is similar to the thermal conductivity of other open framework materials that show negative or low thermal expansion, including ZrW_2O_8 [9] and HfMo_2O_8 [10]. The low thermal conductivity could be a delimiter for applications of such materials in thermal stress management, so we now consider the origins further.

The heat capacity and phonon density of states results showed the prominence of low-frequency optic modes in $\text{Y}_2\text{Mo}_3\text{O}_{12}$. Coupling of the low-frequency optic modes with heat-carrying acoustic modes can lead to low thermal conductivity. We consider the ultimate situation: fully coupled phonons and the corresponding theoretical minimum thermal conductivity, κ_{\min} [36]

$$\kappa_{\min} = \frac{1}{1.24} k_B n^{2/3} v \left(\frac{T}{\theta_D} \right)^2 \int_0^{\theta_D/T} \frac{x^3 e^x}{(e^x - 1)^2} dx, \quad (4)$$

where k_B is Boltzmann's constant, n is the number density, and v is the speed of sound. The result, using $\theta_D = 233$ K (from the experimental velocity of sound; see Supplemental Material [23] for details), is shown in Fig. 4.

The thermal conductivity of $\text{Y}_2\text{Mo}_3\text{O}_{12}$ is low but about an order of magnitude above the minimum value throughout the examined temperature range, indicating that while the system is influenced by the low-frequency optic modes with negative Grüneisen parameters [6] associated with the flexible framework, the phononic interactions do not lead to thermal conductivity as low as in ZrW_2O_8 [9] or in HfMo_2O_8 [10]. The

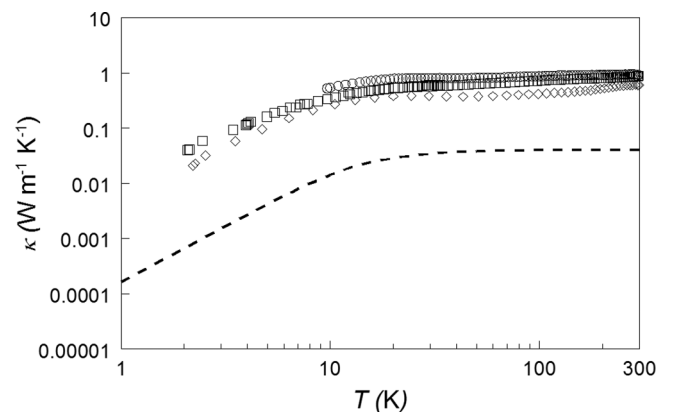


FIG. 4. Temperature dependence of the fully dense thermal conductivity of $\text{Y}_2\text{Mo}_3\text{O}_{12}$ (\circ , E1; \diamond , E2; \square , E3; samples described in Table I); Dashed line denotes the theoretical minimum thermal conductivity.

situation for $Y_2Mo_3O_{12}$ with respect to thermal conductivity is more similar to $HfMgMo_3O_{12}$ [11], although $Y_2Mo_3O_{12}$, ZrW_2O_8 , $HfMo_2O_8$, and $HfMgMo_3O_{12}$ all have about the same calculated minimum theoretical phonon-free path (see Supplemental Material [23]). Despite having flexible framework structures and qualitatively similar phonon density of states for the AM_2O_8 family [37], and the present $A_2M_3O_{12}$ family, namely, a high density of states from ≈ 5 to 350 cm^{-1} and then a gap before the higher energy ($>800\text{ cm}^{-1}$) states, clearly the detailed structure and dynamics are important determiners of the thermal conductivity in these framework materials. Nevertheless, all have low thermal conductivity, especially compared to other ceramics. The difference could lie in the nature of the vibrational modes responsible for NTE, namely, that ZrW_2O_8 has been shown to have rigid unit modes [38], which have negligible vibrational frequency [39]; however, in $A_2M_3O_{12}$ materials, it has been suggested that distortional quasirigid unit modes with nonzero vibrational frequencies [39] cause NTE [4–6].

F. Thermoelasticity

With a good understanding of the thermal and elastic properties of $Y_2Mo_3O_{12}$ and their origins, we now present results from finite-element modeling of the thermal stress in a sample that has undergone a significant change in thermal environment (a temperature drop of 700 K). The thermal stresses, which are caused by the thermal expansion anisotropy and affected by the elastic anisotropy, play an important role in the strength, thermal shock resistance, effective thermal expansion coefficient, and sinterability of the material. The absence of single crystals of $A_2Mo_3O_{12}$ materials prevents experimental determination of the stiffness tensor by Brillouin scattering, so determination of the elastic tensors through computational methods is key.

In the 400 randomly oriented models studied, three related quantities, the first principal invariant of stress (equal to $\sigma_1 + \sigma_2 + \sigma_3$), the strain energy density, and the volumetric strain were found to be normally distributed (see Supplemental Material [23]), as would be the case if elastic anisotropy were not included in the model [25].

The normal distribution of the stress leads to a normal distribution of the strain and therefore a normal distribution of the effective CTE (Fig. 5). The effective CTE is what would be measured experimentally for a bulk sample, if that sample were free of other influences on the CTE, such as microcracking.

A small increase in CTE relative to the experimental intrinsic CTE [5,7] due to coupling of elastic anisotropy with thermal expansion anisotropy [40] can be seen in Fig. 5. Since the experimental CTE tensor was used as an input parameter to the model, if there were no elastic anisotropy, then the effective CTE would equal the experimental CTE. It can be inferred that the increase in CTE is due to the axes with more positive thermal expansion having higher Young's moduli. Note that this effect outweighs that due to the decrease of the axial compressibilities with increasing axial CTE, showing that the crystallites are on average in a state closer to uniaxial stress than isotropic stress.

This finding has consequences regarding the experimental measurement of the elastic properties. Because the relation

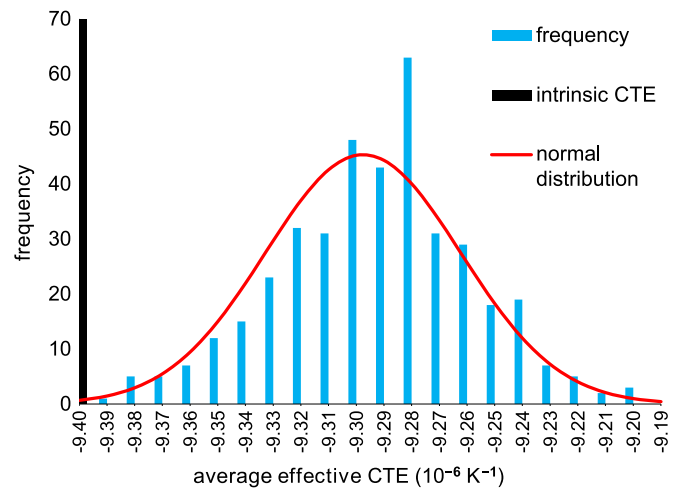


FIG. 5. (Color online) Distribution of the average effective linear CTE for each of the 400 models. A normal distribution is included for comparison. The intrinsic CTE is the experimental value from x-ray diffraction over the temperature range 100 to 900 K [5,7].

between the axial compressibilities (which can be measured by variable-pressure x-ray diffraction) did not, in this case, predict the relation between the axial Young's moduli and because the axial Young's moduli were, in this case, a better predictor of the effective CTE, it is necessary to know the full stiffness tensor.

The expectation values of the various stress measures can be calculated following the method of Kreher [40], but it is more instructive to look at the maxima of various stress measures, as these conditions lead to microcracking and fracture. The maximum and minimum principal stresses are shown in Fig. 6.

The principal stress extrema distributions were fitted using Minitab [41] to three-parameter Weibull distributions, with the probability distribution function

$$P(\sigma) = \gamma\beta^{-\gamma}(\sigma - \sigma_0)^{\gamma-1}e^{-\left(\frac{\sigma - \sigma_0}{\beta}\right)^\gamma}, \quad (5)$$

for $\sigma > \sigma_0$, where σ_0 is the location parameter, β is the scale parameter, and γ is the shape parameter. They are commonly used to describe properties such as maximum stress, strength, and time to failure in cases where some stochastic effect causes them to vary [42–44]. When extrema of the principal stresses are fit, it is appropriate to set σ_0 equal to the smallest value of $|\sigma|$ [43].

The principal stress extrema distributions of Fig. 6 can be compared to those calculated for $Al_2Mo_3O_{12}$ in Ref. [25], using the same method but with isotropic elastic constants. The largest change is in the distributions of the stress extrema from approximately normal to Weibull distributions with $\gamma \approx 2$. A Weibull distribution with $\gamma = 1$ is a normal distribution, while one with $\gamma = 2$ is a Rayleigh distribution. This change in distribution shows that the level of elastic anisotropy in the material will affect the failure behavior of the material [43].

As in $Al_2Mo_3O_{12}$, the distribution of the tensile stresses is broader than that of the compressive stresses [25]. In $Al_2Mo_3O_{12}$, the difference was attributed to two of the crystallographic axes being in tension and one in compression, on average, upon cooling; however, in the case of $Y_2Mo_3O_{12}$ the opposite is true [40]. The broadness of the maximum

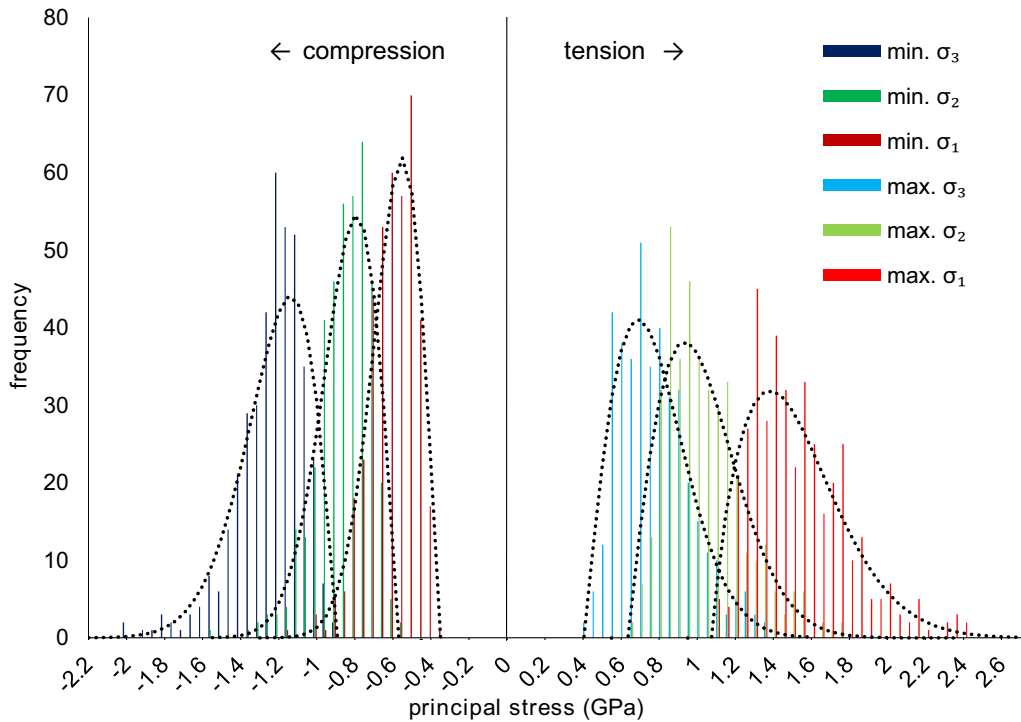


FIG. 6. (Color online) Maxima and minima of the three principal stresses in each of the 400 models. The principal stresses are defined so that $\sigma_1 > \sigma_2 > \sigma_3$. Fitted three-parameter Weibull distributions are shown as dotted lines.

tensile principal stress distribution in $Y_2Mo_3O_{12}$ must be due to another factor, probably the elastic anisotropy. Possibly, the high shear modulus in the plane between the two NTE axes reduces the stress anisotropy in that plane.

The maximum tensile and compressive thermal stresses are defined as the maximum and minimum, respectively, of the first-principal invariant of stress in each model. Both average about 3 GPa, with the maximum tensile stress being more broadly distributed and reaching an ultimate value of 5.5 GPa (see Supplemental Material [23]). These values are very large due to the large amount of CTE anisotropy present in $Y_2Mo_3O_{12}$. Huge tensile stresses of approximately 3 GPa would be enough to cause significant microcracking in the material, while compressive stresses above 2.4 GPa might be sufficient to cause pressure-induced amorphization [45]. The problem of microcracking caused by huge tensile stresses could be mitigated and the strength of the material increased by appropriate control of the particle size and the microstructure of polycrystalline bodies [25].

The thermal stress analysis presented herein has its origins in CTE anisotropy in polycrystalline $Y_2Mo_3O_{12}$; it is proportional to the change in temperature of the material but not the rate of change. If the temperature changes suddenly, additional stress will be present due to thermal shock [46]. The thermal shock a material can withstand decreases with its stiffness and CTE and increases with its fracture strength and thermal conductivity [46]. These properties are all connected to the thermomiotic nature of $Y_2Mo_3O_{12}$.

As we have shown here, $Y_2Mo_3O_{12}$ has low thermal conductivity due to the low-frequency quasirigid unit vibrational modes that are thought to give rise to its NTE, as well as its anomalously high low-temperature heat capacity [33]. Its

high degree of CTE anisotropy can be expected to lead to microcracking in a polycrystalline body, which, in turn, would reduce its fracture strength. $Y_2Mo_3O_{12}$ is relatively compliant for an oxide ceramic, which reduces the amount of thermal stress it experiences but also reduces its strength. Many of these factors are shared with other thermomiotic materials and underscore the challenges involved in their applications.

The effects of elastic anisotropy and its potential connections to CTE anisotropy in thermomiotic materials have not previously been examined closely. In the case of $Y_2Mo_3O_{12}$, the directional shear moduli and compressibilities are strongly anisotropic; however, their effects to some degree cancel, resulting in a different trend in the directional Young's moduli than the compressibilities. The high shear stiffness in the plane between the two axes with large negative CTEs is somewhat surprising given the usual connection between vibrational anharmonicity, thermal expansion, and compliance. This trait can be seen as desirable in applications where a large negative CTE is needed, as it could decrease the material's effective CTE. Whether the trends in the elastic anisotropy seen in $Y_2Mo_3O_{12}$ are shared with other anisotropic thermomiotic materials remains to be seen.

IV. CONCLUSIONS

We have reported the vibrational frequencies, elastic tensor, heat capacity, and thermal conductivity of $Y_2Mo_3O_{12}$; all of these properties are related to its pronounced NTE. Specifically, the structural features that $Y_2Mo_3O_{12}$ shares with other $A_2M_3O_{12}$ materials, namely, an open framework and quasirigid coordination polyhedra, are responsible for the low-frequency vibrational modes that give rise to NTE,

which, in turn, lead to glasslike thermal conductivity and low stiffness. The full anisotropic elastic properties, not previously reported for an $A_2M_3O_{12}$ material, show coupling to the anisotropic thermal expansion properties, which would significantly impact the expected thermal stress distribution. Knowledge of such properties allows prediction of the limits of use of thermomiotic materials in situations involving significant temperature variation.

ACKNOWLEDGMENTS

The authors acknowledge assistance from A. George, Dr. C. Whitman, and Dr. J. Dahn. This study was supported by the Natural Sciences and Engineering Research Council of Canada (NSERC) under Grant No. 1544-2010, the Sumner

Foundation, along with the Canada Foundation for Innovation, and Atlantic Innovation Fund and other partners that fund the Facilities for Materials Characterization managed by the Institute for Research in Materials at Dalhousie University. Computational facilities were provided by the Atlantic Computational Excellence Network (ACEnet), the regional high-performance computing consortium for universities in Atlantic Canada. ACEnet is funded by the Canada Foundation for Innovation, the Atlantic Canada Opportunities Agency, and the provinces of Newfoundland and Labrador, Nova Scotia, and New Brunswick. B. A. Marinkovic is grateful to the Brazilian National Council for Scientific and Technological Development for Research Productivity Grant under Grant No. 304256/2012-9.

-
- [1] C. P. Romao, K. J. Miller, C. A. Whitman, M. A. White, and B. A. Marinkovic, in *Comprehensive Inorganic Chemistry II*, edited by J. Reedijk and K. Poepplmeier (Elsevier, Oxford, 2013), Vol. 4, pp. 128–151.
- [2] C. Lind, *Materials* **5**, 1125 (2012).
- [3] T. A. Mary, J. S. O. Evans, T. Vogt, and A. W. Sleight, *Science* **272**, 90 (1996).
- [4] E. Liang, H. Huo, J. Wang, and M. J. Chao, *J. Phys. Chem. C* **112**, 6577 (2008).
- [5] B. A. Marinkovic, M. Ari, R. de Avillez, F. Rizzo, F. F. Ferreira, K. J. Miller, M. B. Johnson, and M. A. White, *Chem. Mater.* **21**, 2886 (2009).
- [6] L. Wang, F. Wang, P.-F. Yuan, Q. Sun, E.-J. Liang, Y. Jia, and Z.-X. Guo, *Mater. Res. Bull.* **48**, 2724 (2013).
- [7] B. A. Marinkovic, P. M. Jardim, R. R. de Avillez, and F. Rizzo, *Solid State Sci.* **7**, 1377 (2005).
- [8] K. J. Miller, C. P. Romao, M. Bieringer, B. A. Marinkovic, L. Prisco, and M. A. White, *J. Am. Ceram. Soc.* **96**, 561 (2013).
- [9] C. A. Kennedy and M. A. White, *Solid State Commun.* **134**, 271 (2005).
- [10] C. A. Kennedy, M. A. White, A. P. Wilkinson, and T. Varga, *Appl. Phys. Lett.* **90**, 151906 (2007).
- [11] K. J. Miller, M. B. Johnson, M. A. White, and B. A. Marinkovic, *Solid State Commun.* **152**, 1748 (2012).
- [12] S. Sumithra and A. M. Umarji, *Mater. Res. Bull.* **40**, 167 (2005).
- [13] S. D. Gates and C. J. Lind, *J. Solid State Chem.* **180**, 3510 (2007).
- [14] C. A. Kennedy, M. Stancescu, R. A. Marriott, and M. A. White, *Cryogenics* **47**, 107 (2007).
- [15] O. Maldonado, *Cryogenics* **32**, 908 (1992).
- [16] X. Gonze, B. Amadon, P.-M. Anglade, J.-M. Beuken, F. Bottin, P. Boulanger, F. Bruneval, D. Caliste, R. Caracas, M. Cote, T. Deutsch, L. Genovese, Ph. Ghosez, M. Giantomassi, S. Goedecker, D. Hamann, P. Hermet, F. Jollet, G. Jomard, S. Leroux *et al.*, *Phys. Commun.* **180**, 2582 (2009).
- [17] X. Gonze, J.-M. Beuken, R. Caracas, F. Detraux, M. Fuchs, G.-M. Rignanese, L. Sindic, M. Verstraete, G. Zerah, F. Jollet, M. Torrent, A. Roy, M. Mikami, Ph. Ghosez, J.-Y. Raty, and D. C. Allan, *Comp. Mater. Sci.* **25**, 478 (2002).
- [18] ABINIT, <http://www.abinit.org>, accessed July 14, 2014.
- [19] J. W. Zwanziger, *Phys. Rev. B* **76**, 052102 (2007).
- [20] J. P. Perdew, K. Burke, and M. Ernzerhof, *Phys. Rev. Lett.* **77**, 3865 (1996).
- [21] D. R. Hamann, *Phys. Rev. B* **88**, 085117 (2013).
- [22] <http://opium.sourceforge.net/>, accessed July 14, 2014.
- [23] See Supplemental Material at <http://link.aps.org/supplemental/10.1103/PhysRevB.90.024305> for calculated vibrational frequencies, phonon dispersion curves, heat capacity data and models, thermal conductivity data, phonon mean free path, finite-element analysis of thermal stress.
- [24] COMSOL Multiphysics, Burlington, MA.
- [25] L. P. Prisco, C. P. Romao, M. A. White, and B. A. Marinkovic, *J. Mater. Sci.* **48**, 2986 (2013).
- [26] A. C. Torres Dias, C. Luz Lima, W. Paraguassu, K. Pereira da Silva, P. T. C. Freire, J. Mendes Filho, B. Marinkovic, K. J. Miller, M. A. White, and A. G. Souza Filho, *Vib. Spectrosc.* **68**, 251 (2013).
- [27] S. G. Lekhnitskii, *Theory of Elasticity of an Anisotropic Elastic Body* (Holden-Day Inc., San Francisco, 1963).
- [28] T. Varga, A. P. Wilkinson, C. Lind, W. A. Bassett, and C.-S. Zha, *Phys. Rev. B* **71**, 214106 (2005).
- [29] J. S. O. Evans, T. A. Mary, and A. W. Sleight, *J. Solid State Chem.* **137**, 148 (1998).
- [30] M. Asmani, C. Kermel, A. Leriche, and M. Ourak, *J. Eur. Ceram. Soc.* **21**, 1081 (2001).
- [31] F. R. Drymiotis, H. Ledbetter, J. B. Betts, T. Kimura, J. C. Lashley, A. Migliori, A. P. Ramirez, G. R. Kowach, and J. Van Duijn, *Phys. Rev. Lett.* **93**, 025502 (2004).
- [32] L. Qui and M. A. White, *J. Chem. Educ.* **78**, 1076 (2001).
- [33] M. B. Jakubinek, C. A. Whitman, and M. A. White, *J. Therm. Anal. Calorim.* **99**, 165 (2010).
- [34] P. G. Klemens, *High Temp. High Press.* **23**, 241 (1991).
- [35] C. Bryan, C. A. Whitman, M. B. Johnson, J. F. Niven, P. Murray, A. Bourque, H. A. Dąbkowska, B. D. Gaulin, and M. A. White, *Phys. Rev. B* **86**, 054303 (2012).
- [36] D. G. Cahill and R. O. Pohl, *Annu. Rev. Phys. Chem.* **39**, 93 (1988).
- [37] G. Ernst, C. Broholm, G. R. Kowach, and A. P. Ramirez, *Nature (London)* **396**, 147 (1998).

- [38] M. G. Tucker, A. L. Goodwin, M. T. Dove, D. A. Keen, S. A. Wells, and J. S. O. Evans, *Phys. Rev. Lett.* **95**, 255501 (2005).
- [39] A. K. A. Pryde, K. D. Hammonds, M. T. Dove, V. Heine, J. D. Gale, and M. C. Warren, *J. Phys.: Condens. Matter* **8**, 10973 (1996).
- [40] W. S. Kreher, *Comp. Mater. Sci.* **7**, 147 (1996).
- [41] Minitab, www.minitab.com, accessed July 14, 2014.
- [42] W. Weibull, *J. Appl. Mech. Trans. ASME* **18**, 293 (1951).
- [43] X. Chen and T. D. Papathanasiou, *Compos. Sci. Technol.* **64**, 1101 (2004).
- [44] D. Cousineau, *IEEE Trans. Dielectr. Electr. Insul.* **16**, 281 (2009).
- [45] T. Varga, A. P. Wilkinson, C. Lind, W. A. Bassett, and C.-S. Zha, *J. Phys. Cond. Matt.* **17**, 4271 (2005).
- [46] T. J. Lu and N. A. Fleck, *Acta Mater.* **46**, 4755 (1998).